Saturation of the Internal Tides and Induced Mixing in the Abyssal Ocean

CAROLINE J. MULLER* AND OLIVER BÜHLER

Courant Institute of Mathematical Sciences, New York University, New York, New York

ABSTRACT

As part of an ongoing effort to develop a parameterization of wave-induced abyssal mixing, the authors derive an heuristic model for nonlinear wave breaking and energy dissipation associated with internal tides. Then the saturation and dissipation of internal tides for idealized and observed topography samples are investigated. One of the main results is that the wave-induced mixing could be more intense and more confined to the bottom than previously assumed in numerical models. Furthermore, in this model wave breaking and mixing clearly depend on the small scales of the topography below 10 km or so, which is below the current resolution of global bathymetry. This motivates the use of a statistical approach to represent the unresolved topography when addressing the role of internal tides in mixing the deep ocean.

1. Introduction

The presence of celestial bodies induces a barotropic current in the ocean, known as the barotropic tide. This barotropic tide interacts with the seafloor in the presence of stratification, resulting in the radiation of internal waves. This process is known as tidal conversion and the resulting internal waves are known as the *internal tides*. These internal tides propagate from the seafloor and can become unstable and break. As they break, they contribute to vertical mixing; this could explain measurements of high diapycnal diffusivities over the rough bathymetry of the Mid-Atlantic Ridge where diapycnal diffusivity can reach several orders of magnitude higher than the background value $0.1 \text{ cm}^2 \text{ s}^{-1}$ (e.g., Polzin et al. 1997; Ledwell et al. 2000). This tidal mixing is currently believed to be important for the dynamics of the large-scale ocean circulation as a whole, especially in the deep, abyssal ocean below 1500-m depth or so (e.g., Munk and Wunsch 1998; Wunsch 2000; and the reviews in Wunsch and Ferrari 2004 and Thorpe 2005). As

much as 1 TW of tidal energy could be converted to internal tides in the deep ocean (Egbert and Ray 2000, 2001). Tidal mixing at depth may also play an important role in homogenizing water masses of different origin, such as North Atlantic Deep Water and Antarctic Bottom Water.

How is this tidal abyssal mixing distributed, both horizontally and vertically? How does it affect general circulation models (GCMs) used for climate prediction? These questions are all the more relevant because GCMs have been shown to be sensitive to diffusivity values (e.g., Samelson 1998). These internal wave processes are far too small in spatial and temporal scale to be resolved in GCMs, and therefore theory and observations must be used to parameterize them. At present, there is little theory to guide these parameterizations, in particular as far as the distribution of wave breaking in the vertical is concerned. Previous studies have focused on the conversion rate, which is the rate of conversion of energy from the barotropic tide into the internal tides upon generation of the waves at the seafloor (e.g., Cox and Sandstrom 1962; Robinson 1969; Baines 1973; Bell 1975a,c; Llewellyn Smith and Young 2002; Khatiwala 2003; St. Laurent and Garrett 2002; St. Laurent et al. 2003; Balmforth et al. 2002; Llewellyn Smith and Young 2003; Di Lorenzo et al. 2006; Petrelis et al. 2006; Legg and Huijts 2006; see also Garrett and Kunze 2007 for a recent review). But very little is known about where and when this energy contributes to mixing as internal tides propagate, become unstable, and break.

* Current affiliation: Department of Earth, Atmospheric and Planetary Sciences, Massachusetts Institute of Technology, Cambridge, Massachusetts.

Corresponding author address: Caroline J. Muller, Department of Earth, Atmospheric and Planetary Sciences, Massachusetts Institute of Technology, Cambridge, MA 02139.
E-mail: muellerc@mit.edu

A comprehensive understanding of internal tides and of their role in the ocean circulation must encompass an understanding of their generation, instability, and eventual breakdown into three-dimensional turbulence. In Bühler and Muller (2007, henceforth BM07), we investigate the generation and instability of internal tides in a very simple linear model that allows us to relate the formation of unstable regions to simple features in the seafloor topography. Interestingly, for three-dimensional tides over two-dimensional topography, there can be geometric focusing of wave energy into localized regions of high wave amplitude. Overall, the distribution of unstable wave breaking regions can be highly nonuniform even for very simple idealized topography shapes. We interpret these instability regions as the seeds of the three-dimensional turbulence that ultimately produces the small-scale mixing that is relevant to the ocean circulation.

This paper aims to understand the instability and turbulent dissipation of the internal tides. In other words, we address the following questions: how much energy is lost by the internal tides when they saturate and break? How is the induced mixing distributed in the vertical? To answer these questions, we introduce a new heuristic method to estimate tidal mixing above the abyssal seafloor, which we refer to as the *saturation scheme*. Briefly, we derive a parameterization that models both the linear propagation as well as the nonlinear saturation and breaking of the waves, which allows us to estimate the dissipation in regions of wave breaking.

Then we use this saturation scheme to investigate the tidal wave field generated by random topography with simple isotropic homogeneous spectrum proposed by Bell (1975b) (see also Müller and Xu 1992) using Monte Carlo simulations. The simple spectrum proposed by Bell lacks inhomogeneity and the presence of deterministic features, but it gives us insight into the statistics of large-amplitude regions and implied vertical diffusivity. Despite the simplicity of our model, we find profiles of energy flux and vertical diffusivity consistent with oceanic measurements, decreasing from $\mathcal{O}(10 \text{ cm}^2 \text{ s}^{-1})$ to 1 cm^2 s^{-1} within the first 500–600 m, and then decreasing to its background value of $\mathcal{O}(0.1 \text{ cm}^2 \text{ s}^{-1})$ higher up in the water column. An interesting finding is that the wave-induced mixing could be more intense and more confined to the bottom than previously assumed.

Finally, we apply these results to local topographic data on the Mid-Atlantic Ridge. It turns out that the presence of instabilities in the wave field depends heavily on the small scales of the topography, below 10 km or so. This implies that a complete understanding of ocean mixing would require knowledge of the bathymetry well below the current resolution (Smith and Sandwell 1997).

There are several nondimensional parameters in this problem. The first one is the ratio ϵ of the topography slope to the characteristics slope of the internal waves. Topographies in the range $0 \leq \epsilon < 1$ are known as subcritical topographies, $\epsilon = 1$ corresponds to critical topography, and topographies for which $\epsilon > 1$ are known as supercritical topographies. Here we focus on gentle, widespread subcritical topographies such as features of the Mid-Atlantic Ridge; that is, we assume $\epsilon < 1$. This is motivated by convenience and by the surprising fact that the simplest linear theory for subcritical topography delivers results that are qualitatively reasonable and accurate compared to numerical estimates of energy conversion rate within a factor of 2 or so. Using altimetry data, Egbert and Ray (2000) identify areas of the deep ocean associated with strong tidal conversion. These fall into two categories: steep tall topographic features such as the Hawaiian Ridge ($\epsilon > 1$) and gentle widespread topography such as regions near the Mid-Atlantic Ridge ($\epsilon < 1$). The first category has been the subject of an extensive observational study, namely, the Hawaii Ocean Mixing Experiment (HOME) (see, e.g., Rudnick et al. 2003; the June 2006 issue of *Journal of Physical Oceanography*; see also Garrett and Kunze 2007 for a review). As mentioned above, we focus here on the second category of topographies. Unfortunately, there are very few measurements near subcritical topography in the deep ocean, although vertical profiles of diapycnal diffusivity near the Mid-Atlantic Ridge were computed during the Brazil Basin Tracer Release Experiment (e.g., Toole et al. 1994; Polzin et al. 1997; Ledwell et al. 2000).

The second nondimensional parameter is the so-called tidal excursion $U_0 k/\omega_0$, which compares the gradient length scale of the topography $1/k$ with the distance U_0/ω_0 covered by the barotropic tide, where U_0 denotes the amplitude of the tidal velocity and ω_0 denotes the tidal frequency. Typically in the deep ocean, the tidal excursion is small. For instance, with $U_0 = \mathcal{O}(3 \text{ cm s}^{-1})$ and $\omega_0 = 1.4 \times 10^{-4}$ s^{-1} for the semidiurnal tide (see Bell 1975c), $U_0/\omega_0 = \mathcal{O}(200 \text{ m})$, which is smaller than most topographic features of interest. Nevertheless we do *not* use the common small excursion approximation ($U_0 k/\omega_0 \ll 1$), since this approximation overestimates contributions from small scales (see, e.g., St. Laurent and Garrett 2002; BM07), and the topographies considered here can contain significant small-scale roughness. But we still neglect higher harmonics; that is, we only consider the waves at the tidal frequency ω_0, which dominate the wave field for small excursions. We note in passing that the other limit $U_0 k/\omega_0 \gg 1$ corresponds to the case of lee waves generated by stationary currents. This is, for instance, the relevant regime for the interaction between mesoscale eddies and the seafloor.

TABLE 1. Notations.

(x, y) horizontal coordinates	z vertical coordinate
N buoyancy frequency	f Coriolis parameter
$\omega_0 > 0$ tidal frequency	$\mathbf{U} = (U_0 \cos\omega_0 t, V_0 \sin\omega_0 t, 0)$ tidal ellipse (velocity of the barotropic tide)
$\hat{h}(k) = FT\{h\}(k) = \int_{-\infty}^{\infty} h(x)e^{-\imath kx}\,dx$	Fourier transform and inverse Fourier transform (two-dimensional waves above one-dimensional topography)
$h(x) = FT^{-1}\{\hat{h}\}(x) = \dfrac{1}{2\pi}\int_{-\infty}^{\infty} \hat{h}(k)e^{\imath kx}\,dk$	
$\mathbf{x} = x,\ \mathbf{r} = |x|,\ \mathbf{k} = k,\ \boldsymbol{\kappa} = |k|$	
$\hat{h}(\mathbf{k}) = FT\{h\}(\mathbf{k}) = \int_{-\infty}^{\infty}\int_{-\infty}^{\infty} h(\mathbf{x})e^{-\imath \mathbf{k}\cdot\mathbf{x}}\,dx\,dy$	Fourier transform and inverse Fourier transform (three-dimensional waves above two-dimensional topography)
$h(\mathbf{x}) = FT^{-1}\{\hat{h}\}(\mathbf{x}) = \dfrac{1}{(2\pi)^2}\int_{-\infty}^{\infty}\int_{-\infty}^{\infty} \hat{h}(\mathbf{k})e^{\imath \mathbf{k}\cdot\mathbf{x}}\,dk\,dl$	
$\mathbf{x} = (x,y),\ r = \sqrt{x^2 + y^2},\ \mathbf{k} = (k,l),\ \kappa = \sqrt{k^2 + l^2}$	

In this work, we only consider wave energy dissipation through instabilities with fast time scales, such as convective or shear instabilities, near the generation site. There are other sinks of internal tides energy such as scattering by the bottom (Müller and Xu 1992) and the thermocline (Gerkema 2001), nonlinear wave–wave interactions including parametric subharmonic instability (St. Laurent and Garrett 2002; Alford et al. 2007), critical reflection (Kunze and Llewellyn Smith 2004), and scattering by mesoscale features (Rainville and Pinkel 2006). These mechanisms typically have longer time scales and act on the low-mode internal tides that radiate away from the generation site. The ultimate fate of these low-mode internal tides that can propagate over 1000 km from generation sites is still an open question and is beyond the scope of this study.

The paper is laid out as follows: in section 2 we discuss the vertical structure and instability of the linear internal tides. In section 3 we add to the linear theory a parameterization for nonlinear wave breaking and energy dissipation, which allows us to investigate the saturation and dissipation of internal tides for simple random topographies described in section 4. Then in section 5, we apply our results to a local topography spectrum of the Mid-Atlantic Ridge; this highlights the role of small-scale topography in the abyssal wave-induced mixing. In section 6 we discuss the effects of finite ocean depth on our results, and concluding remarks are offered in section 7.

2. Internal tides: The linear solution

We consider the linear waves generated by the flow of a uniformly stratified fluid with barotropic tidal velocity $\mathbf{U}(t)$ over infinitesimal seafloor topography $z = h(x, y)$ (see Table 1 for the various notations). We consider a linear Boussinesq model with constant buoyancy frequency N and Coriolis parameter f and infinite vertical extent. For simplicity, this omits all effects to do with variable stratification and finite ocean depth; in particular it omits wave reflection in the vertical. We will discuss finite-depth effects in section 6.

a. Vertical structure of the internal tides in two dimensions

In this section we consider the two-dimensional problem in the xz plane such that $\partial/\partial y = 0$ for all fields including the bottom topography $h(x)$. We will come back to the less-studied three-dimensional case in the next section. The internal tides at fundamental frequency ω_0 have vertical velocity (see, e.g., Bell 1975a; Khatiwala 2003; BM07 for details; see Table 1 for notations)

$$w(x, z, t) = \text{Re}\{W(x,z)e^{-i\omega_0 t}\}$$

with $\quad W(x,z) = G(x,z) * W(x,0), \quad \hat{G}(k,z) = e^{-i|k|\mu z}$

and $\quad \hat{W}(k,0) = 2i\omega_0 J_1\!\left(\dfrac{U_0 k}{\omega_0}\right)\hat{h}(k),$ (1)

where $J_1(x)$ is the Bessel function of the first kind of order 1, the asterisk (*) denotes convolution in x, and μ is given by

$$\mu = \left|\frac{m}{k}\right| = \sqrt{\frac{N^2 - \omega_0^2}{\omega_0^2 - f^2}}. \qquad (2)$$

From (1) we see that the vertical structure of the internal tides is extremely simple and is governed by an operator G. This is true for the vertical velocity as well as any other function of the wave field: an x convolution with the operator $G(x, z)$ provides a map between the

function at the lower boundary $z = 0$ and the function at $z \geq 0$; that is,

$$A(x, z) = G(x, z) * A(x, 0)$$
$$\Leftrightarrow \hat{A}(k, z) = \exp(-i|k|\mu z)\hat{A}(k, 0) \quad (3)$$

holds for any complex wave field A defined in analogy with W in (1). In fact, there is nothing special about the location $z = 0$ because (3b) makes obvious that G satisfies the group property $G(x, z_1 + z_2) = G(x, z_1) * G(x, z_2)$ for arbitrary z_1 and z_2. Thus, we can view G as the unique linear operator that maps wave fields between different depths.

Time-periodic internal waves are peculiar because their spatial structure is governed by a hyperbolic equation (e.g., Sobolev 1960; Maas and Lam 1995) whose characteristics indeed coincide with the usual group-velocity rays. The slope of the group-velocity rays is $dz/dx = \pm\mu^{-1}$. Typically in the deep ocean μ takes moderate values of order unity. For instance, for the M_2 tide $\omega_0 = 1.4 \times 10^{-4}$ s^{-1}, and with the representative near bottom buoyancy frequency $N = 5f - 10f$ and $f = \omega_0/2$ at a latitude of 30°, $\mu = 2.6 - 5.7$ therefore the slope $dz/dx = \mu^{-1}$ is about a quarter or so. In the upper ocean N is about 10 times bigger and the slope flattens correspondingly.

The conversion of energy per unit length in y from the barotropic tide to internal tides upon generation is given by the time-averaged vertical energy flux EF at $z = 0$:

$$\text{EF}(z = 0) = \frac{\rho_0 \omega_0 \sqrt{N^2 - \omega_0^2}\sqrt{\omega_0^2 - f^2}}{\pi}$$
$$\times \int_{-\infty}^{\infty} \frac{J_1^2(U_0 k/\omega_0)|\hat{h}(k)|^2}{|k|} dk. \quad (4)$$

This energy conversion rate quantifies the mean energy flux of the internal tides, which presumably is ultimately related to the deep-ocean mixing caused by dissipating or breaking internal tides.

b. Vertical structure of the internal tides in three dimensions

We now turn to the less-studied three-dimensional problem with tidal ellipse $\mathbf{U} = (U_0 \cos\omega_0 t, V_0 \sin\omega_0 t, 0)$ and topography $h(x, y)$. The case of elliptic forcing without the small excursion approximation has been studied by Bell (1975c) who computed the bottom energy flux, but to the best of our knowledge the full solution has not yet been given so we include a detailed derivation in the appendix. The tidal ellipse enters the solution through its boundary condition, which for the vertical velocity yields (see Table 1 for notations)

$$w(\mathbf{x}, z, t) = \text{Re}\{W(\mathbf{x}, z)e^{-i\omega_0 t}\}$$

with

$$W(\mathbf{x}, z) = G(\mathbf{x}, z) * W(\mathbf{x}, 0), \quad \hat{G}(\mathbf{k}, z) = e^{-i\kappa\mu z} \quad \text{and}$$

$$\hat{W}(\mathbf{k}, 0) = 2i\omega_0\hat{h}(\mathbf{k})\frac{J_1(\sqrt{U_0^2 K^2 + V_0^2 L^2}/\omega_0)}{\sqrt{U_0^2 K^2 + V_0^2 L^2}}$$
$$\times e^{iV_0 L/\omega_0}(KU_0 + iLV_0), \quad (5)$$

where $J_1(x)$ is the Bessel function of the first kind of order 1, the asterisk (*) denotes convolution in $\mathbf{x} = (x, y)$, and μ is given by (2). Here $(K, L) = (k\cos\alpha - l\sin\alpha, k\sin\alpha + l\cos\alpha)$ is the wavenumber vector in the frame of the tidal ellipse (Fig. 10). As in the two-dimensional case, the vertical structure of the internal tides is entirely governed by an operator G; that is,

$$A(\mathbf{x}, z_2) = G(\mathbf{x}, z_2 - z_1) * A(\mathbf{x}, z_1)$$
$$\Leftrightarrow \hat{A}(\mathbf{k}, z_2) = e^{-i\kappa\mu(z_2 - z_1)}\hat{A}(\mathbf{k}, z_1). \quad (6)$$

The rate of conversion of energy from the barotropic tide into the internal tides is given by the time-averaged vertical energy flux EF at $z = 0$:

$$\text{EF}(z = 0) = \frac{\rho_0 \omega_0 \sqrt{N^2 - \omega_0^2}\sqrt{\omega_0^2 - f^2}}{2\pi^2}\int_{-\infty}^{\infty}\int_{-\infty}^{\infty} \frac{J_1^2(\sqrt{U_0^2 K^2 + V_0^2 L^2}/\omega_0)|\hat{h}(\mathbf{k})|^2}{\kappa} dk \, dl. \quad (7)$$

c. Instabilities of the wave field

We now investigate the instability of the internal tides. We simultaneously address the two-dimensional and three-dimensional problems with the unifying notations $\mathbf{x} = x, \mathbf{k} = k$, and $\kappa = |k|$ in two dimensions and $\mathbf{x} = (x, y)$, $\mathbf{k} = (k, l)$, and $\kappa = \sqrt{k^2 + l^2}$ in three dimensions. Following BM07, we use a simple measure of wave amplitude

based either on Kelvin–Helmholtz instability flagged by low Richardson number or based on convective instability flagged by negative stratification. With Coriolis forces and three-dimensional flows it is simpler to look at the latter and therefore we look at the stratification surfaces of constant $\Theta = b + N^2 z$, which is proportional to the materially conserved density in the Boussinesq model for the ocean. Here $b = -g(\rho - \rho_s(z))/\rho_0$ is the usual buoyancy

disturbance given in terms of gravity g, density ρ, constant reference density ρ_0, and the linear background stratification $\rho_s(z) = \rho_0(1 - N^2 z/g)$. Negative stratification corresponds to overturning of the stratification surfaces such that $\partial\Theta/\partial z$ is negative. We find, as in BM07,

$$\frac{\partial\Theta}{\partial z} \propto 1 - \mathrm{Re}[e^{-i\omega_0 t} A(\mathbf{x}, z)]$$

$$A(\mathbf{x}, z) = G(\mathbf{x}, z) * A(\mathbf{x}, 0), \tag{8}$$

where $\hat{A}(k, 0) = 2i\kappa\mu\hat{h}(k)J_1(U_0 k/\omega_0)$ in two dimensions and $\hat{A}(\mathbf{k}, 0) = 2i\kappa\mu\hat{h}(\mathbf{k})[J_1(\sqrt{U_0^2 K^2 + V_0^2 L^2}/\omega_0)/\sqrt{U_0^2 K^2 + V_0^2 L^2}]e^{iV_0 L/\omega_0}(KU_0 + iLV_0)$ in three dimensions.

This introduces the nondimensional wave amplitude $A(\mathbf{x}, z)$ and $|A| > 1$ signals convective instability at some point in the oscillation.

We can recover any other function of the linear wave field from the amplitude through the following relations derived from the equations of motion (see, e.g., Bell 1975c; BM07):

$$\hat{u} = \frac{\omega_0}{k}\hat{A}, \quad \hat{v} = -i\frac{f}{k}\hat{A}, \quad \hat{w} = \frac{\omega_0}{\mu\kappa}\hat{A},$$

$$\hat{p} = \frac{\rho_0(\omega_0^2 - f^2)}{\kappa^2}\hat{A}, \quad \hat{b} = -i\frac{N^2}{\mu\kappa}\hat{A} \tag{9}$$

in two dimensions and

$$\hat{u} = \frac{\omega_0 k + fil}{\kappa^2}\hat{A}, \quad \hat{v} = \frac{\omega_0 l - fik}{\kappa^2}\hat{A}, \quad \hat{w} = \frac{\omega_0}{\mu\kappa}\hat{A},$$

$$\hat{p} = \frac{\rho_0(\omega_0^2 - f^2)}{\kappa^2}\hat{A}, \quad \hat{b} = -i\frac{N^2}{\mu\kappa}\hat{A} \tag{10}$$

in three dimensions.

3. Nonlinear saturation of the internal tides

In this section, we use the operator G of the previous section to derive a parameterization for nonlinear wave saturation and breaking, which allows us to estimate the energy dissipation due to breaking internal tides. Saturation is a classical idea used in wave-drag parameterizations in the atmosphere, but all previous saturation models are based on ray tracing and therefore the relevant wave amplitude is the magnitude of a monochromatic plane wave that forms the core of a slowly varying wave train. Here we propose a new algorithm to allow for the local saturation of the internal tides that is not based on ray tracing; that is, we do not assume a slowly varying wave train and therefore we deal with a wave amplitude field that is not related to plane waves.

This is the main difference to the classical wave saturation schemes.

In the following we simultaneously address the two- and three-dimensional problems. Our flag for wave instabilities is the wave amplitude A in (8). Whenever and wherever $|A| > 1$, the waves are unstable and break. So our model for wave breaking is based on the following idea: solving the linear equations but under the constraint $|A| \leq 1$. In other words, we solve for the linear wave field subject to the constraint that the waves are stable everywhere. This is a heuristic model for what, presumably, happens in nonlinear reality: when the wave amplitude exceeds unity the waves become unstable, break, and at the end of this process the wave field has stabilized. We combine this simple nonlinear saturation idea with linear vertical wave propagation as follows: recall that the vertical structure of the liner waves is governed by the operator G in (6), which maps any function A of the wave field at a level z_1 to the function at a level z_2. The saturation scheme consists of the following: start at $z = 0$, saturate the amplitude $A(\mathbf{x}, z)$ at depth z, that is, enforce $|A(\mathbf{x}, z)| \leq 1$ for all $\mathbf{x}$, and propagate the saturated amplitude to the next level $z + dz$ by convolution with the operator $G(dz)$. In other words, the saturation scheme consists in saturating, propagating up, saturating, propagating up, etc. In this manner, we obtain the saturated wave amplitude everywhere and we can recover any other function of the wave field through (9) and (10). The only thing remaining to complete the saturation scheme is a way to enforce $|A| \leq 1$.

The first natural idea is to define a nonlinear saturation of amplitude, with the saturated amplitude given by

$$A_s = A + \left(\frac{A}{|A|} - A\right)\chi_{|A|>1},$$

$$= \begin{cases} A & \text{if} \quad |A| \leq 1 \\ \dfrac{A}{|A|} & \text{if} \quad |A| > 1 \end{cases}, \tag{11}$$

where χ denotes the indicator function. It indeed saturates the waves wherever A reaches unity and enforces $|A| \leq 1$. But unfortunately this is not entirely satisfactory, because the relations between A and the other functions of the wave field are nonlocal. This nonlocality can be seen from the $1/\kappa$ and $1/\kappa^2$ factors in (9) and (10), which correspond to convolutions with $\ln r$ and r in two dimensions and with $1/r$ and $\ln r$ in three dimensions. So a local change in A due to wave breaking yields a global change in pressure, which is unphysical (this is illustrated through an example in Fig. 1). Another way to view this problem is that, mathematically, as a linear wave field the function $A(x, y, z)$ must have zero-mean value when integrated over the horizontal coordinates,
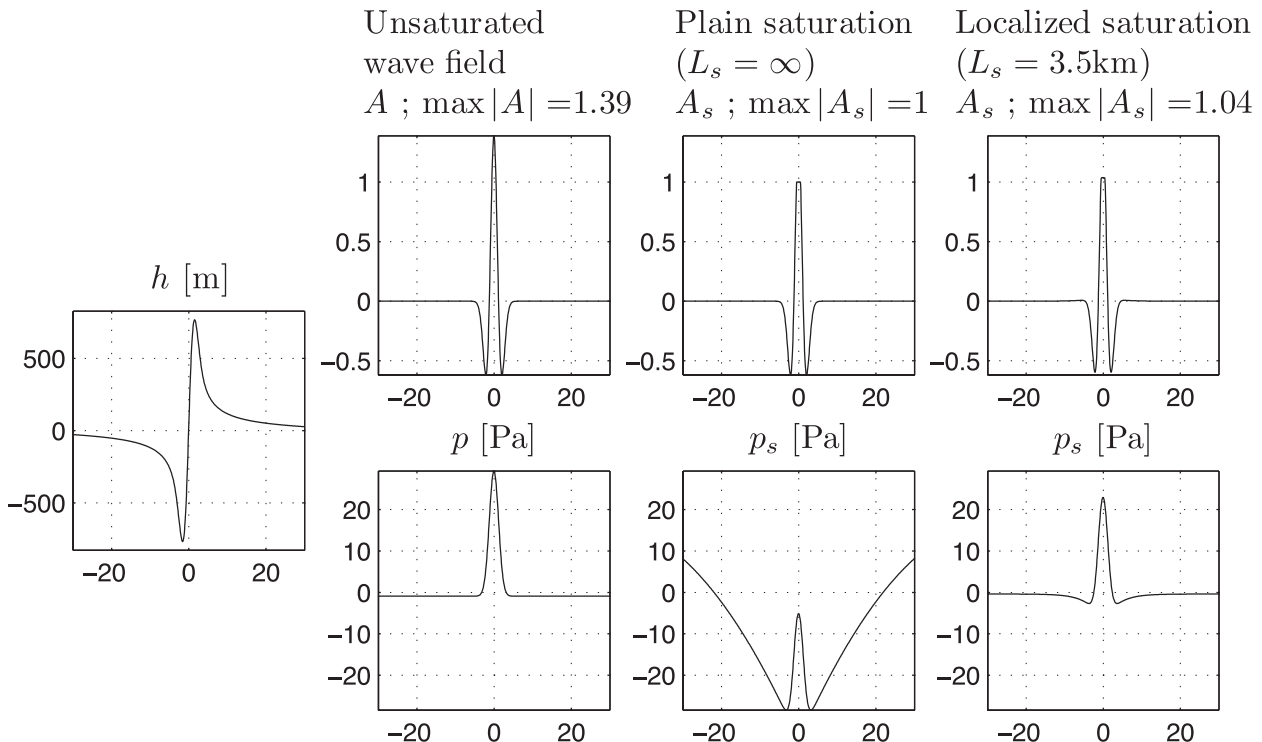
FIG. 1. Plain saturation vs localized saturation.

and this is violated by (11). Ideally, we would like the saturation to be localized near instabilities for all functions of the wave field. We achieve this by introducing the localized saturation

$$A_s = A + \left(\frac{A}{|A|} - A\right)\chi_{|A|>1} * g, \quad \hat{g} = \frac{\kappa^2}{\kappa^2 + L_s^{-2}}. \quad (12)$$

The Fourier transform of g is almost $\equiv 1$ at scales small compared to L_s, but at large sales $\kappa < L_s^{-1}$, $\hat{g} = \mathcal{O}(\kappa^2)$. Convolution with g ensures that all functions of the wave field still look like localized wavy perturbations after saturation, with zero horizontal average. In fact, in two dimensions, $g = \delta(x) - e^{-|x|/L_s}/(2L_s)$, where $\delta(x)$ denotes the Dirac delta function, so convolution with g corresponds to subtracting a weighted local average $(f*g)(x) = f(x) - 1/(2L_s)\int f(x')e^{-|x-x'|/L_s} dx' \sim f(x) - 1/(2L_s)\int_{x-L_s}^{x+L_s} f(x') dx'$. For finite L_s, convolution with g heals the nonlocality of the plain saturation, as illustrated in Fig. 1. Unfortunately, it introduces a free parameter, namely, the saturation length L_s.

We propose an ad hoc fix for the value of this free parameter by minimizing the bottom energy flux [given by (4) in two dimensions and (7) in three dimensions] of the saturated wave field, consistent with the intuition that saturation and wave breaking should decrease the wave energy. We will go through the detailed compu-

tation of L_s in three dimensions in section 4 once we have introduced Bell's topography spectrum. Briefly, without saturation, the internal tides associated with a reasonable choice of random topography have an energy flux upon generation at $z = 0$ of 2 mW m^{-2} (see Fig. 3). We then compute the saturated internal tides using (12), and find that the energy flux at $z = 0$ is minimum for the value of the parameter $L_s = 5$ km (Fig. 3). A similar computation in two dimensions, using a one-dimensional equivalent of Bell's topography spectrum, yields $L_s = 3.5$ km. To summarize, the saturation scheme is

start at $z = 0$;
saturate the amplitude $A(\mathbf{x}, z)$ at a given z using (12);
propagate the saturated amplitude to the next level $z + dz$ by convolution with the operator $G(dz)$.

We illustrate this saturation scheme using the same example as BM07, namely, a piecewise quadratic topography, which yields an unstable wave field as observed on the left panel of Fig. 2. The right panel shows the saturated wave field. When saturation is applied, most of the overturning of the buoyancy surfaces is suppressed. Note that with L_s finite we do not exactly enforce $|A| \leq 1$ everywhere, so there can still be some instabilities. Nevertheless, saturation ensures a significant reduction of the unstable amplitude, so overall the saturated wave field is very close to being stable.
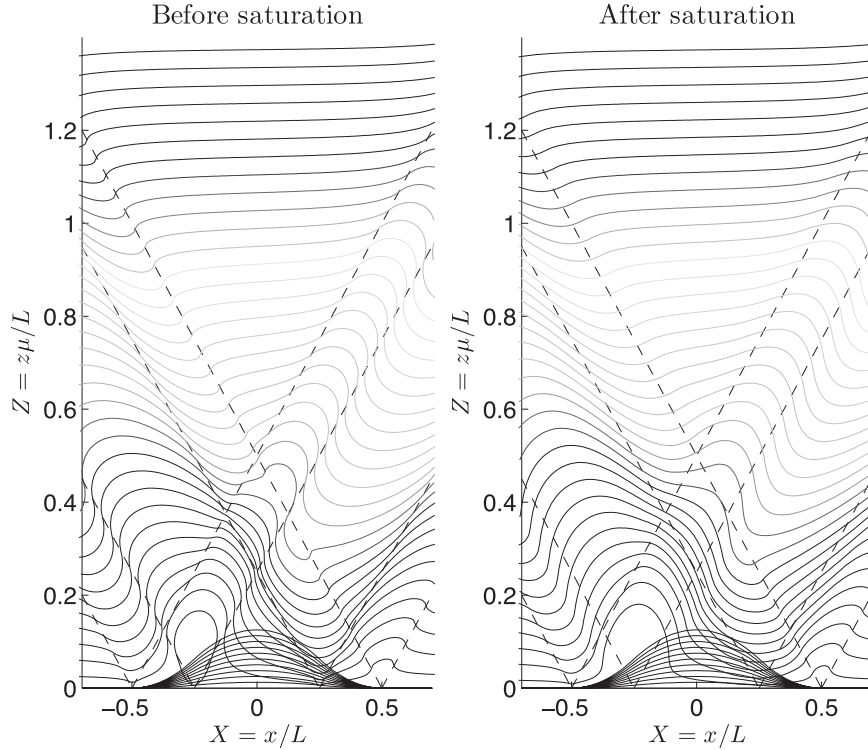
Before saturation   After saturation

FIG. 2. Buoyancy surfaces with saturation.

4. Tidal mixing over random topography

a. Random topography and bottom energy flux

Our knowledge of the seafloor is rather poor, especially at scales below 40 km or so (Smith and Sandwell 1997), which leads us to take a statistical approach. We use the simplest model for the topography, namely, a random Gaussian field. We are not aware of specific evidence whether small-scale seafloor topography can be modeled as a Gaussian field, but Gaussian fields are certainly a convenient starting point. Importantly, internal tides forced by Gaussian topographies are themselves a three-dimensional Gaussian random field, which makes all the standard tools available for their study.

We use the simple topography spectrum proposed by Bell (1975b) (see also Müller and Xu 1992). This spectrum is isotropic with a power law such that the variance of h is

$$ \mathbb{E}(h^2) = (125 \text{ m})^2 \int_0^{\kappa_2} \frac{\kappa_1 \kappa}{(\kappa^2 + \kappa_1^2)^{3/2}} \, d\kappa, \qquad (13) $$

with parameters $(\kappa_1, \kappa_2) = (2\pi/40 \text{ km}, 2\pi/400 \text{ m})$, where $\mathbb{E}$ denotes the expected value. The cutoff parameter κ_2 regulates the slope variance $\mathbb{E}(|\nabla h|^2) = (125 \text{ m})^2 \kappa_1 \kappa_2 \approx (0.2)^2$. Using Bell's spectrum and our assumption that the topography is a random Gaussian field, we can generate

samples of the topography. Note that there is no tunable parameter in the generation of the topography.

There are other statistical representations of the seafloor. Goff and Jordan (1988) have proposed an anisotropic spectrum with five parameters that can be tuned to best match the available data in a region. We will look in detail at a region near the Mid-Atlantic Ridge in section 5, so we could use their spectrum with the parameters from their Atlantic data. Nevertheless, the Atlantic region is the area where their model does most poorly. Becker and Sandwell (2008) have also been working on a global map of seafloor slope. In this paper, we will focus on simple isotropic spectra.

We model the barotropic tide with the unidirectional velocity $\mathbf{U}(t) = (U_0 \cos\omega_0 t, 0, 0)$, with semidiurnal values $U_0 = 4 \text{ cm s}^{-1}$, and $\omega_0 = 1.4 \times 10^{-4} \text{ s}^{-1}$. When the barotropic tide $\mathbf{U}(t)$ flows over this topography, internal tides are radiated with energy flux given by (7). The energy flux of the saturated wave field is computed at $z = 0$ for various saturation lengths L_s and is shown in Fig. 3.[1]

---

[1] In this section, the computations are done with a 200 km by 200 km domain, with 1024 grid points in both horizontal directions, and typical vertical resolution $dz = 10$ m. This high horizontal resolution ensures that the wide range of scales of Bell's topography spectrum is well resolved. We use values $f = \omega_0/2$ at a latitude of 30°, and the representative near bottom buoyancy frequency $N = 10f$.

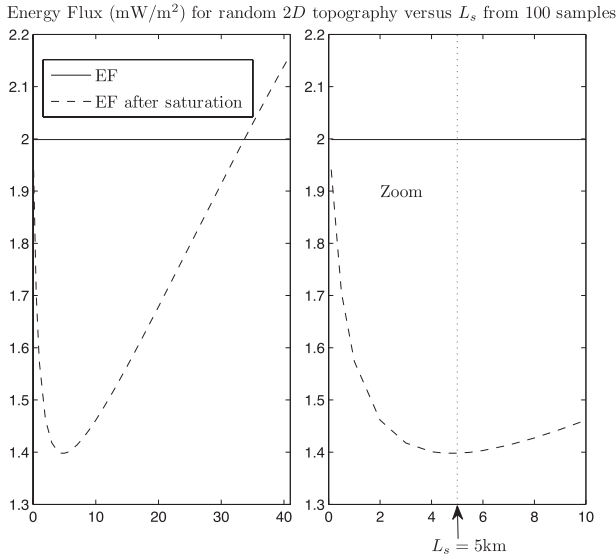Energy Flux (mW/m²) for random 2D topography versus L_s from 100 samples

FIG. 3. Bottom energy flux of the internal tides generated by random topography for various saturation lengths.

As mentioned in section 3, we fix the value of this parameter L_s by minimizing the bottom energy flux after saturation. The energy flux has been computed using Monte Carlo methods with 100 samples. Not surprisingly, because of the nonlocality of the plain saturation, the energy flux diverges as $L_s \to \infty$. In fact, it can be shown that the energy flux diverges linearly in L_s (quadratically for two-dimensional flow). In the other limit $L_s \to 0, g \to 0$ in (12) and we recover the unsaturated energy flux. Between these two limits, the bottom energy flux has a minimum at $L_s = 5$ km. This is the value that we will use in the saturation scheme.

b. Vertical profiles of energy flux and implied diffusivity

The vertical profiles of energy flux, energy dissipation and implied vertical diffusivity for random topography with Bell's spectrum before and after saturation are shown in Fig. 4, computed using Monte Carlo methods with 100 samples. The energy flux (EF in $W\,m^{-2}$), energy dissipation (ϵ in $W\,m^{-3}$), and vertical diffusivity (K in $m^2\,s^{-1}$) are all horizontal averages, so

$$\epsilon = -\frac{\partial \text{EF}}{\partial z}.$$

We use the Osborn–Cox model (Osborn and Cox 1972) to deduce the vertical profile of mixing:

$$K = \frac{\Gamma \epsilon}{\rho N^2}$$

with a mixing efficiency $\Gamma = 0.2$.

A first interesting result is that there are instabilities in the wave field. This is not an obvious result. In fact, we find that $\mathbb{E}|A|^2 = (0.84)^2$ yielding $|A| > 1$ on 23% of the domain. An important point to make here is that using the small excursion approximation would yield unrealistically large amplitudes, with variance larger than 4. This approximation is based on the observation that, in the deep ocean, the tidal excursion U_0/ω_0 is small compared to most topographic features of interest (e.g., for the M_2 tide, $U_0/\omega_0 \approx 4\ \text{cm s}^{-1}/1.4 \times 10^{-4}\ \text{s}^{-1} \approx 300\ \text{m}$, which is indeed small). Physically this means that advection by the barotropic tide can be neglected, and mathematically it implies that the Bessel function is replaced by its small argument limit $J_1(x) \sim_{x \ll 1} x/2$ in (5). This approximation is accurate at large scales, but it overestimates contributions from small scales where the correct estimate is $J_1(x) \sim_{x \gg 1} 1/\sqrt{x}$. For instance, for the amplitude, the small excursion approximation yields $\hat{A}(\mathbf{k}) = _{\kappa \gg 1} \mathcal{O}(\kappa^2)$ when the correct estimate at small scales from (8) is $\hat{A}(\mathbf{k}) = _{\kappa \gg 1} \mathcal{O}(\sqrt{\kappa})$. Therefore the small excursion approximation overestimates contributions from small scales. This remark holds for the energy flux as well, with Fourier transform $\propto |\hat{A}|^2/\kappa^3 = _{\kappa \gg 1} \mathcal{O}(\kappa)$ in the small excursion approximation, when the correct estimate is $\mathcal{O}(1/\kappa^2)$. This makes it clear that one should *not* use the small excursion approximation to correctly represent small-scale contributions. This is especially important for topographies with significant small-scale roughness.

Without saturation, the energy flux is constant with height (since the operator G is unitary) and is equal to $2\ \text{mW m}^{-2}$. Note that if we multiply this value by the total area of the oceans, we obtain a total dissipation of $(2\ \text{mW m}^{-2})(360 \times 10^6\ \text{km}^2) \approx 0.7\ \text{TW} = \mathcal{O}(1\ \text{TW})$, which is of the same order as the energetics derived from satellite data (Egbert and Ray 2000, 2001). With saturation, the energy flux is found to decrease with height and its vertical profile is well approximated by the function (Fig. 4)

$$\text{EF}(z) \approx \text{EF}_{\text{app}} = \begin{cases} 1.4\ \text{mW m}^{-2} & \text{for } z < 35\ \text{m} \\ 0.7 + e^{-\sqrt{z/300\text{m}}}\ \text{mW m}^{-2} & \text{otherwise} \end{cases}. \tag{14}$$

Approximate functions for the energy dissipation and vertical diffusivity are then $\epsilon_{\text{app}} = -d\text{EF}_{\text{app}}/dz$ and $K_{\text{app}} = \Gamma \epsilon_{\text{app}}/(\rho N^2)$. The energy flux has an interesting profile, at first constant up to ≈ 35 m, and then decreasing with height. Where does this nonmonotonicity come from? And what sets this height of 35 m? It turns out that this height is exactly proportional to the tidal excursion U_0/ω_0 m. In fact, it corresponds to the height at which the imaginary part of the amplitude starts contributing
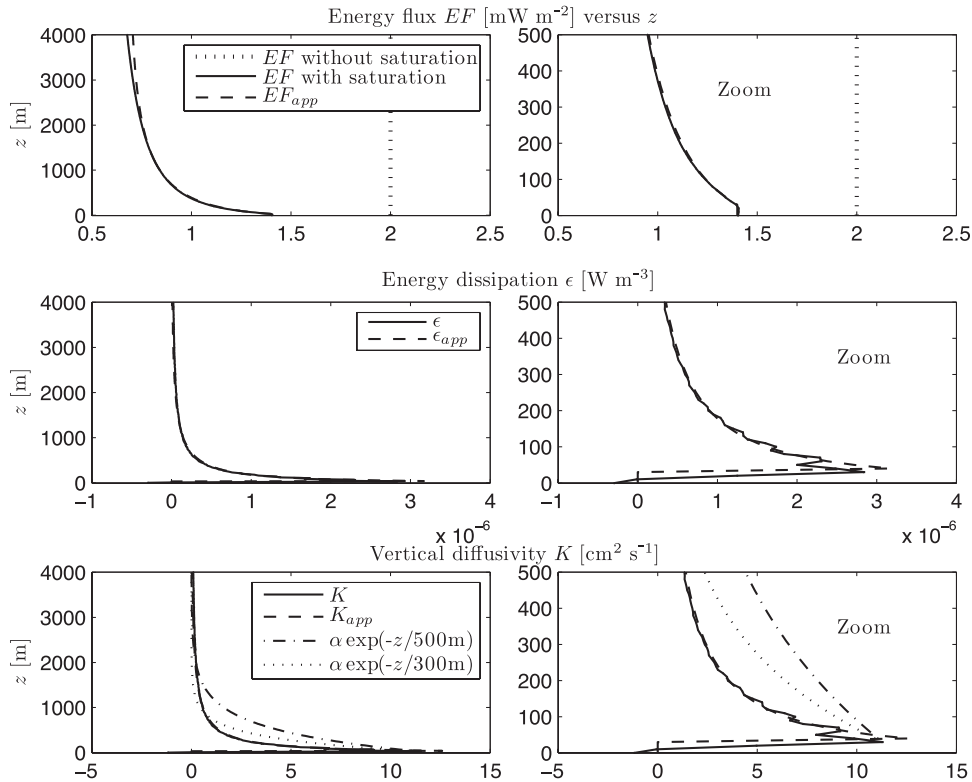
FIG. 4. Energy flux and implied mixing above random topography.

significantly to the solution. Remember that A is real at $z = 0$ from the boundary condition in (8), so

$$A = A_r + iA_i, \quad \hat{A}_r = \hat{A}_0 \cos(\kappa\mu z),$$
$$\hat{A}_i = \hat{A}_0 \sin(\kappa\mu z) = 0 \quad \text{at} \quad z = 0$$

(see scatterplots Fig. 6). At $z = 35$ m, the bottom boundary condition is forgotten and $|A_{\text{sat}}|$ reaches a local maximum (Fig. 7), which corresponds to a peak in the saturation and in the energy dissipation ϵ. We should point out here that, in the real ocean, there are many other processes near the bottom that we have ignored, such as boundary layer effects. Our computation isolates the effect of tides, and in reality we do not expect the diffusivity to be zero at the seafloor.

We note in passing that the amplitude of the waves based on shear instability ($\sqrt{u_z^2 + v_z^2}/N$) has a similar vertical profile as our amplitude based on convective instability, with a local maximum near $z = 35$ m. Depending on the critical Richardson number used, shear instabilities are either negligible ($\text{Ri}_{\text{crit}} = \frac{1}{4}$) or yield similar profiles ($\text{Ri}_{\text{crit}} = 1$) as convective instabilities. Also, we have checked that our results do not depend on the vertical resolution by varying the vertical step size dz; for instance, we computed the vertical profile of

diffusivity when the vertical step size is increased from 10 to 25 m (Fig. 8). There is a slight loss of detail near the bottom because of the lower resolution, but overall the profiles are very similar, which gives us confidence that our results do not depend on the vertical resolution.

Despite the simplicity of our model, we find a profile of diffusivity in good agreement with oceanic measurements, decreasing from $\mathcal{O}(10\ \text{cm}^2\ \text{s}^{-1})$ to $\mathcal{O}(1\ \text{cm}^2\ \text{s}^{-1})$ within 600 m, and then to its background value of $0.1\ \text{cm}^2\ \text{s}^{-1}$ higher up in the water column, as is most easily seen on a logarithmic plot in Fig. 5 (see, e.g., Polzin et al. 1997 for measurements of vertical diffusivity above the Mid-Atlantic Ridge). An interesting finding is that the tidal mixing could be more confined to the bottom than previously assumed. Indeed, previous parameterizations used exponential decay of diffusivity from the bottom with a decay scale of 500 m (e.g., St. Laurent et al. 2002; Simmons et al. 2004; Saenko and Merryfield 2005; Canuto et al. 2009, manuscript submitted to *Ocean Modell.*), but we find that near the bottom diffusivity decays with height faster than exponential. Even if we decrease the decay scale to 300 m, the agreement is not greatly improved. Beyond 2 km, this statement is reversed and diffusivity decays slower than exponential.

Furthermore, the current consensus seems to be that most of the energy flux radiates away as low modes, but
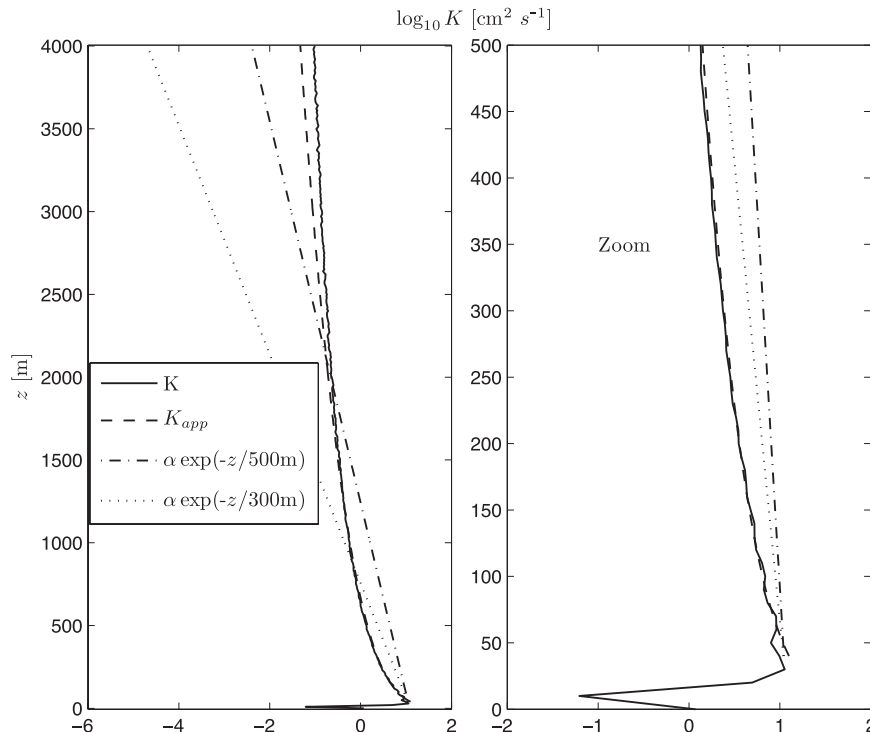
$\log_{10} K$ [cm^2 s^{-1}]

FIG. 5. Logarithmic plot of vertical diffusivity above random topography.

our results indicate that as much as 65% of the energy flux could get dissipated during the generation process. Indeed, without saturation the energy flux is 2 mW m^{-2}, and with saturation only 0.7 mW m^{-2} radiate away to $z \to \infty$, yielding a total loss of 65% of which 30% is lost directly at the generation site and 60% within the first kilometer of the water column. Therefore localized mixing above topographic features of significant roughness could be more confined to the bottom and more intense than currently believed.

c. Model robustness

Interestingly, and perhaps surprisingly, the far-field value obtained, $K \to 0.1$ cm^2 s^{-1} as $z \to \infty$, agrees with measurements of pelagic vertical diffusivity. We checked if this result is sensitive to the only parameter of the saturation scheme, namely, L_s in (12). Earlier in this section we fixed the value for this parameter by minimizing the energy flux of the saturated wave field at the seafloor, and found $L_s = 5$ km. We computed the mean and standard deviation of K averaged over the last 500 m of the water column, allowing L_s to vary from 1 to 15 km. The results are summarized in Table 2. It turns out that the result is robust: the mean of the pelagic diffusivity obtained is not sensitive to the value of the parameter L_s, although deviations from this mean increase as L_s increases, that is, as the nonlocality of the saturation increases.

5. Application to the Mid-Atlantic Ridge

a. Smith and Sandwell bathymetry

In the previous sections, we focused on a statistical representation of the bathymetry, using Bell's homogeneous isotropic spectrum to generate random Gaussian fields with realistic statistics. This gave us insight into the statistics of large-amplitude regions and implied diffusivity, but although the real bathymetry might be close to isotropic and homogeneous at small scales, it is likely not the case at large scales. In this section, we will look at a local topography near the Mid-Atlantic Ridge (MAR), obtained from the global bathymetry from Smith and Sandwell (1997). We therefore expect this observational topography to be anisotropic and inhomogeneous. St. Laurent and Garrett (2002) studied in detail the generation of internal tides in the region of the MAR shown in Fig. 9, and we will use the same region to study wave instabilities and wave-induced mixing.

Since the tidal ellipse does not vary much over the region considered (Fig. 9) we use the average ellipse $\mathbf{U}(t) = [U_0 \cos(\omega_0 t), V_0 \sin(\omega_0 t), 0]$ given in Fig. 10 (adapted from St. Laurent and Garrett 2002). Tidal ellipse parameters are taken from St. Laurent and Garrett (2002) as well as other parameters shown in Fig. 10. Bathymetry data are taken from Smith and Sandwell (1997), using Hann windowing to compute the Fourier
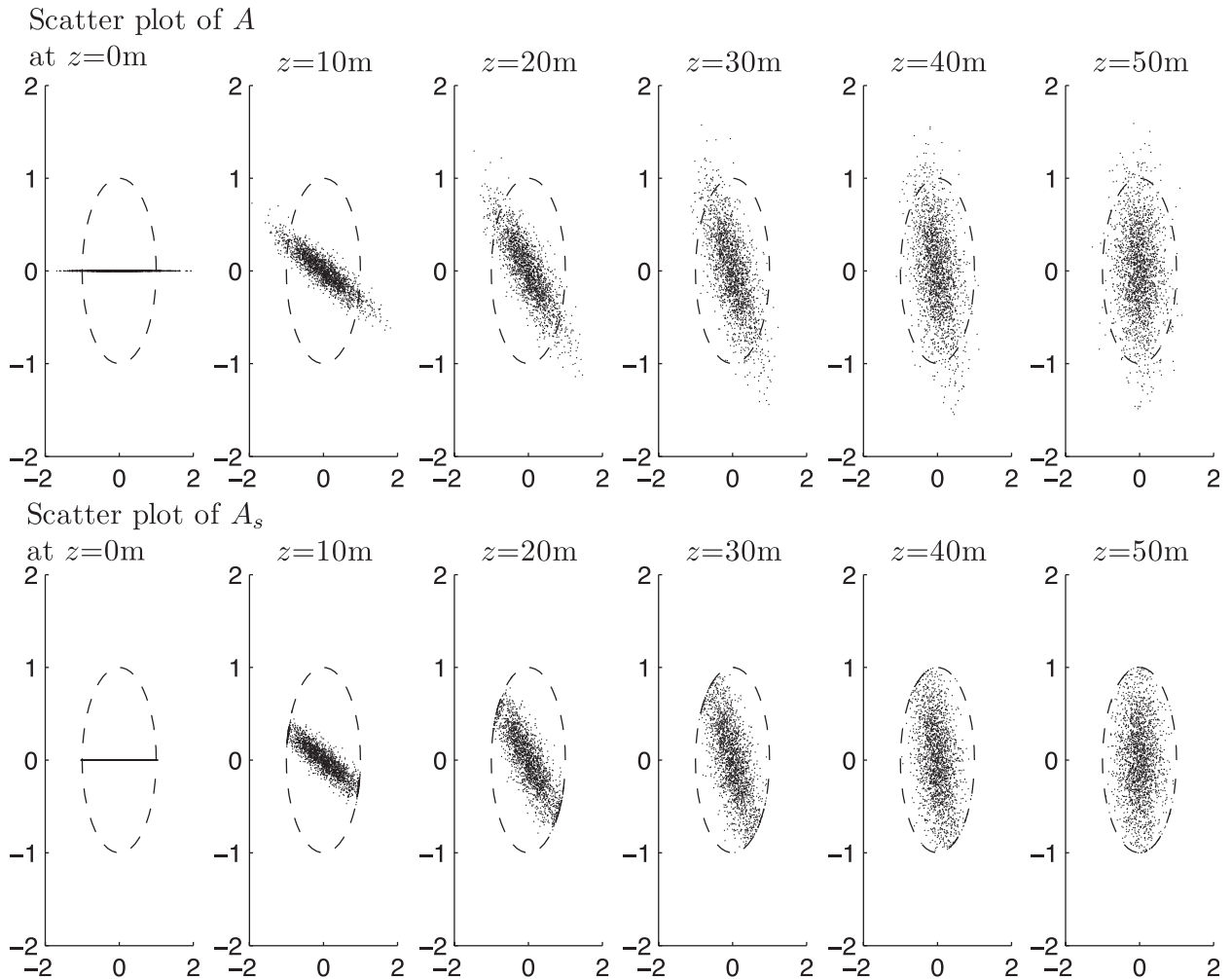
Scatter plot of A

Scatter plot of A_s

FIG. 6. Scatterplot of the wave amplitude above random topography.

transform. This global bathymetry has grid size $dx = \mathcal{O}(2\ \text{km})$ (although it does not resolve topographic scales below 40 km or so).

We applied the saturation scheme to the waves generated above this MAR site and obtained the vertical profile of vertical diffusivity shown in Fig. 11. We find that there is hardly any energy loss, and the diffusivity is equal to or smaller than the background value 0.1 cm^2 s^{-1} throughout the water column. So what happens? Does saturation really yield no mixing above the MAR? It turns out that that the small scales of the topography, below 10 km, are crucial for the presence of instabilities and mixing in the wave field. The lack of small scales in the Smith and Sandwell (1997) bathymetry yields very little mixing, with diffusivities close to the background value. In fact, if we go back to the random topography of section 4 and remove scales below 10 km by reducing the large-scale cutoff κ_2 in the spectrum (13), there is no saturation at all and the diffusivity is 0. This is because

saturation occurs precisely when and where the amplitude exceeds unity and the amplitude is sensitive to small topographic scales. In fact, for Bell's spectrum, it can be shown that the variance of amplitude increases as $\ln\kappa_2$ as $\kappa_2 \to \infty$ (Fig. 12). A logarithmic dependence is not a strong dependence, but for small values of κ_2 the variance of amplitude decreases rapidly to zero, yielding very little or no saturation.

b. Multibeam bathymetry

How can we estimate the energy dissipation and implied diffusivity above the MAR? From the results of the previous section, we need information about the seafloor at scales smaller than the Smith and Sandwell (1997) resolution. High-resolution multibeam data are available for parts of this MAR region (St. Laurent and Garrett 2002). In this section we use the multibeam bathymetry to fit a power-law spectrum similar to Bell's. Then, within the limits of isotropic spectrum, we can
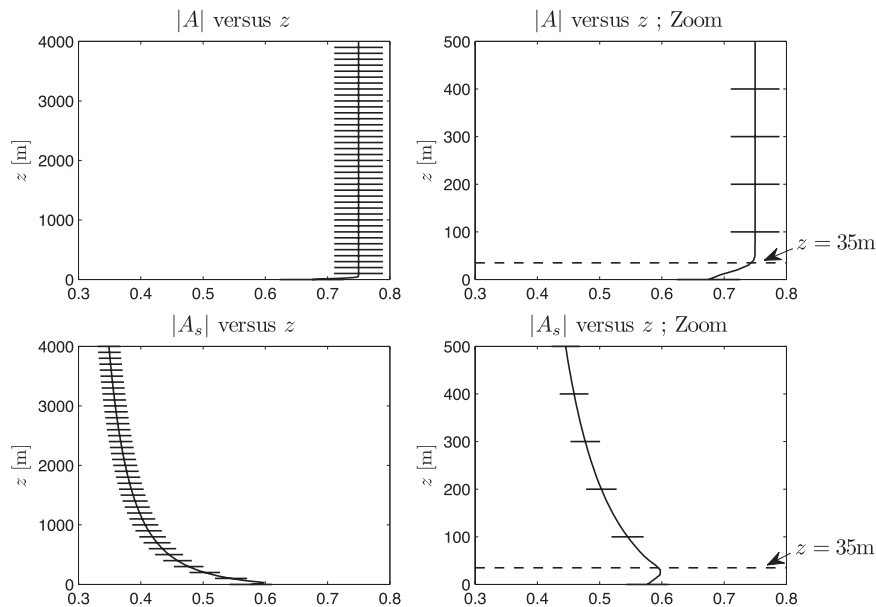
FIG. 7. Vertical profile of the modulus of wave amplitude above random topography.

generate topography samples consistent with the multibeam data and use the saturation scheme to compute the corresponding profiles of energy flux and vertical diffusivity.

Since the multibeam spectrum is given for one-dimensional topography $h(x)$, we first need to derive the one-dimensional equivalent to Bell's spectrum. For a stationary random process $h(x, y)$ isotropic spectrum $\mathbb{E}[h(x', y')h(x' + x, y' + y)] = C(x, y) = C(\sqrt{x^2 + y^2})$, there is a simple relationship between the one-dimensional and the two-dimensional spectra $\hat{c}(k) = 2\int_0^\infty \hat{C}(k, l)dl/(2\pi)$ (this is equivalent to the somewhat more complicated
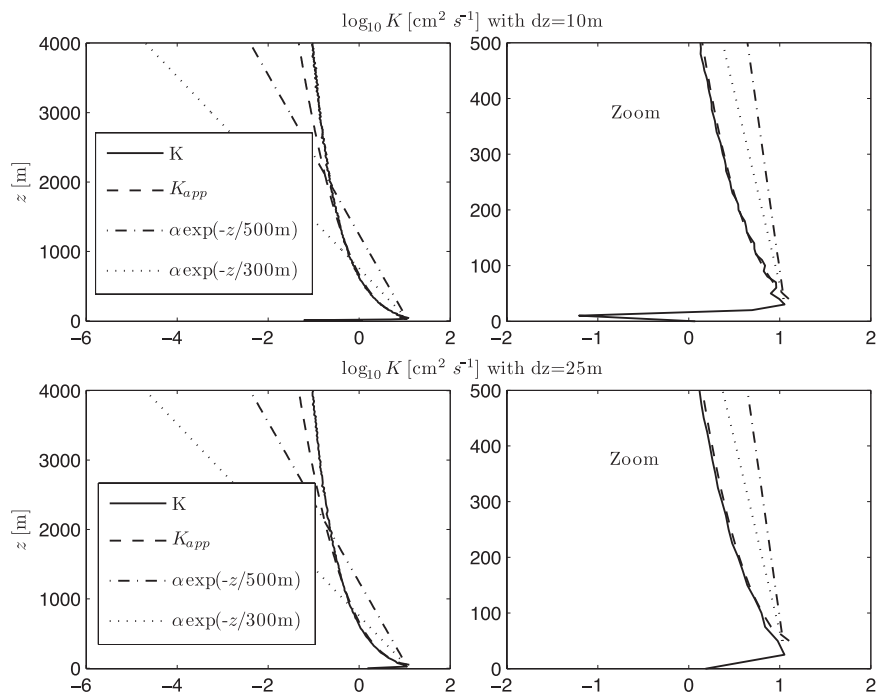

FIG. 8. Same as in Fig. 5, but with different vertical resolution.

TABLE 2. Mean and standard deviation of the far-field vertical diffusivity (K in cm^2 s^{-1} averaged over the last 500 m of the water column 3500 m $\leq z \leq$ 4000 m) for various values of the parameter L_s in (12). The mean K agrees well with oceanic measurements of pelagic vertical diffusivity, and this result is not sensitive to the value of the parameter. But deviations from this mean increase with L_s, i.e., as the nonlocality of the saturation increases.

L_s	Mean K	Std dev of K
1 km	0.08	0.01
5 km	0.10	0.07
10 km	0.11	0.18
15 km	0.12	0.32

formula given by Bell 1975b). For Bell's spectrum (13), this yields the one-dimensional spectrum

$$\hat{c}(k) = (125 \text{ m})^2 \frac{2\kappa_1 \chi_{|k| \leq \kappa_2} \sqrt{\kappa_2^2 - k^2}}{\sqrt{\kappa_2^2 + \kappa_1^2}(k^2 + \kappa_1^2)}. \qquad (15)$$

In particular, the spectral slope at large wavenumbers increases from -3 for two-dimensional topography to -2 for one-dimensional topography.

Figure 13 shows Bell's one-dimensional spectrum as well as the observed spectrum over the MAR in two directions: across the fracture zone (XFZ direction) and along the fracture zone (FZ direction; see St. Laurent and Garrett 2002 for details). Somewhat surprisingly, the spectra look fairly similar; in particular κ_1 is a reasonable estimate for the round-off wavenumbers in the observed spectrum. Although there is no clear cutoff wavenumber in the multibeam data, κ_2 coincides with the largest wavenumber measured. One difference is the topography variance, which equals $(125 \text{ m})^2$ for Bell's spectrum, $(257 \text{ m})^2$ in the XFZ direction, and $(159 \text{ m})^2$ in the FZ direction, yielding an average variance of about $(200 \text{ m})^2$ for the MAR. Finally, the main difference between the MAR data and Bell's spectrum is the spectral slope at large wavenumbers; the MAR data have a steeper slope of about -2.3 (which corresponds to a spectral slope of -3.3 for two-dimensional topography).
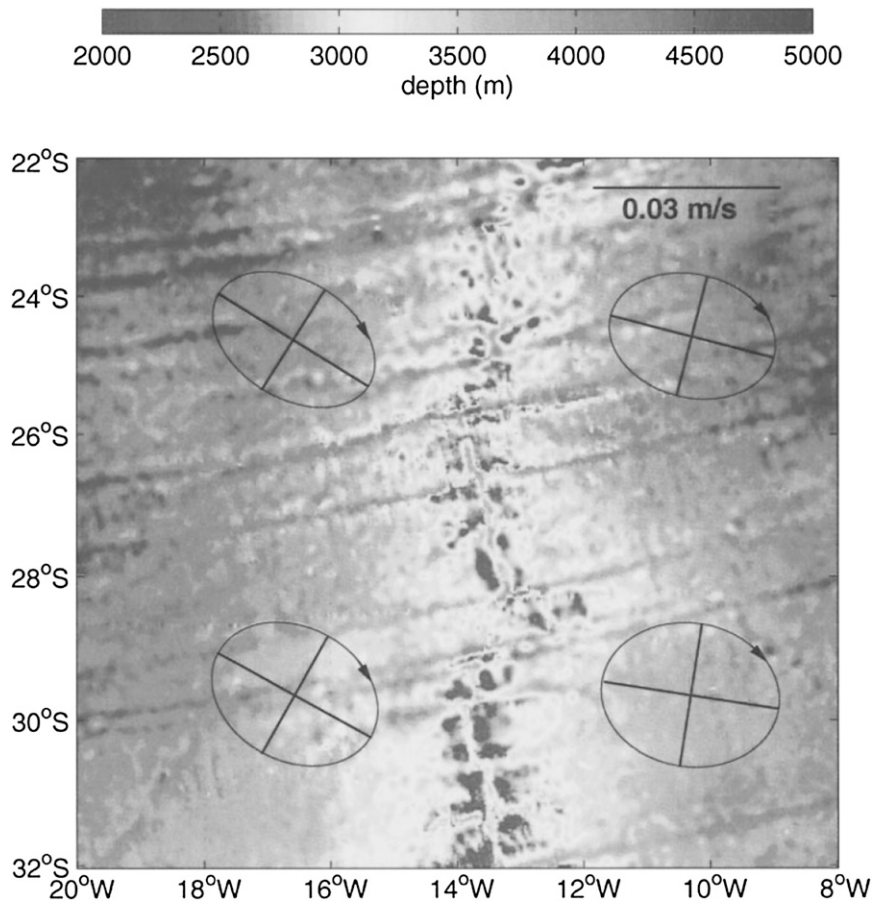

FIG. 9. Map of the region of the Mid-Atlantic Ridge studied in section 5.

$$\alpha = 17^o$$
$$U_0 = 3.3 \text{ cm/s}$$
$$V_0 = -2.34 \text{ cm/s}$$
$$N = 10^{-3} \text{ s}^{-1}$$
$$f = -7.3 \times 10^{-5} \text{ s}^{-1}$$
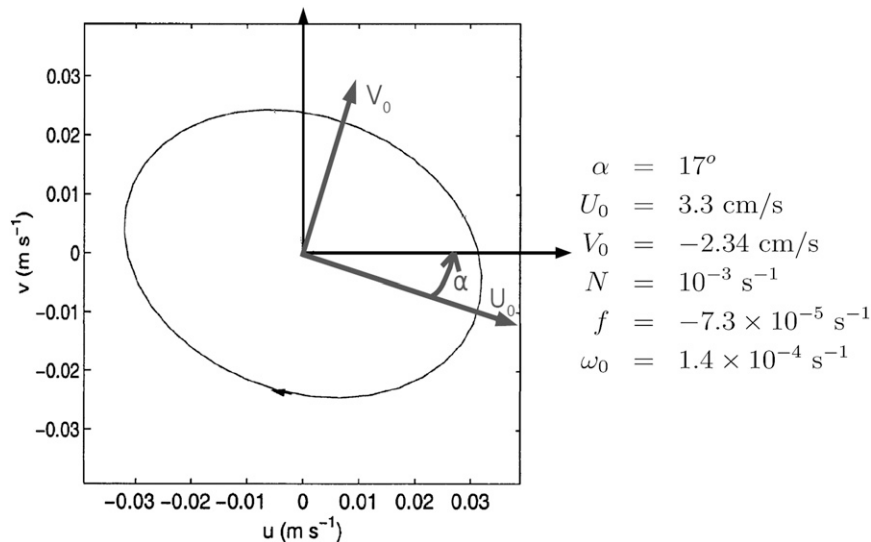$$\omega_0 = 1.4 \times 10^{-4} \text{ s}^{-1}$$

FIG. 10. Average tidal ellipse as well as various parameters at the MAR site (adapted from St. Laurent and Garrett 2002).

So to summarize based on the multibeam data, we modify Bell's two-dimensional spectrum (13), keeping the same values for κ_1 and κ_2 but increasing the topography variance to $\mathbb{E}(h^2) = (200 \text{ m})^2$ and decreasing the slope to -3.3.

Profiles of energy flux, energy dissipation, and vertical diffusivity for this modified Bell's spectrum are shown in Fig. 14. The profiles are very similar to the results obtained with Bell's original spectrum, with twice the values. In fact, if we were to divide all the functions (EF, ϵ and K) by 2, the profiles would fall almost on top of Fig. 4. The two changes in Bell's spectrum have opposite effects: increasing the topography variance leads to higher wave amplitudes and hence more mixing, while decreasing the high-wavenumber spectral slope yields

fewer small scales in the topography and hence less wave saturation and breaking. It turns out that the modified spectrum yields almost the same amplitude variance $\mathbb{E}|A|^2 = (0.86)^2$ as Bell's original spectrum [$\mathbb{E}|A|^2 = (0.84)^2$].

The previously noted fact that there is no clear cutoff wavenumber in the data raises the question of the sensitivity of our results to the high-wavenumber cutoff κ_2. We therefore went back to Bell's original spectrum and changed κ_2 to half κ_2 and twice κ_2 (Fig. 15). When κ_2 is reduced to half its original value, there is much less mixing, as expected since there are fewer small scales
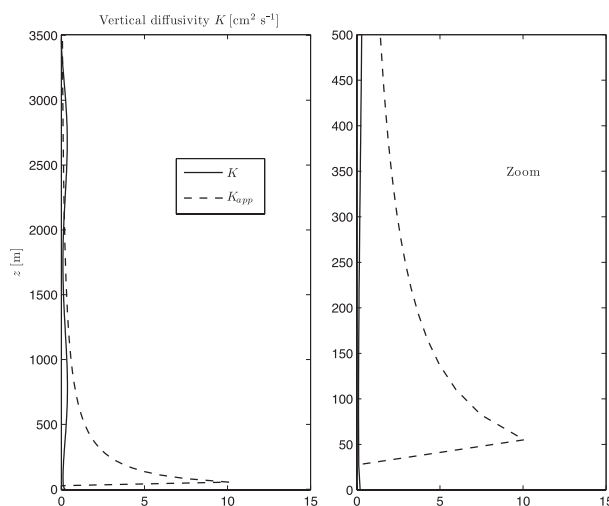

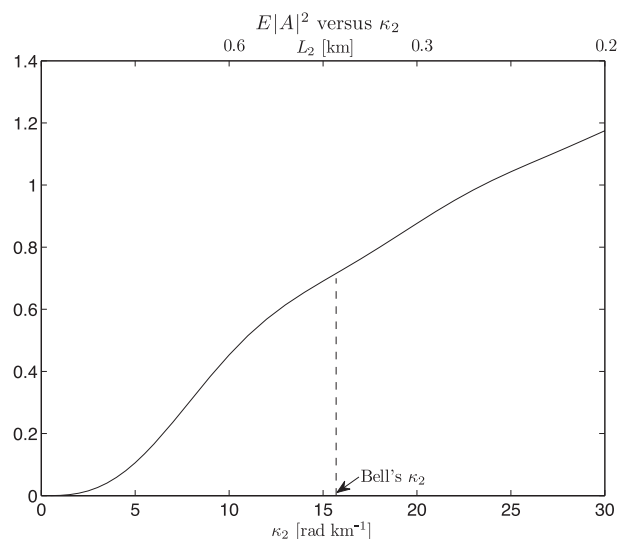FIG. 11. Vertical diffusivity above the Mid-Atlantic Ridge.

FIG. 12. Variance of the wave amplitude vs the high-wavenumber cutoff parameter in Bell's topography spectrum.
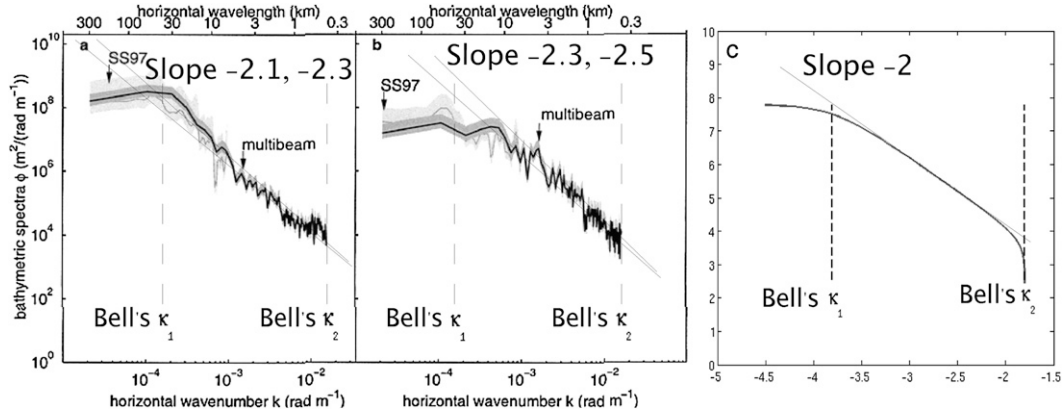
FIG. 13. Bell's one-dimensional topography spectrum and multibeam bathymetry spectrum.

in the topography. When κ_2 is doubled there is more small-scale topography and therefore we expect more instabilities, saturation, and mixing. Indeed, the bottom diffusivity is increased by a factor 2, but the effect is mainly felt in the first 50 m. Beyond this height, we get the same qualitative results as before with the original κ_2. This clarifies the dependence of the results on small topography scales: the presence of small scales is crucial for instabilities and mixing. Nevertheless, as long as κ_2 is greater than a threshold value, there seems to be a robust regime where profiles decay like the analytical fit (14), namely, exponential of root z rather than a simple

exponential decay as previously assumed in numerical models. This result is not exactly true in the first 50 m where bottom values can increase a lot with small-scale roughness, but our model is not accurate near the bottom where boundary layer effects need to be taken into account.

6. A note on finite depth

In an infinitely deep ocean, waves can escape freely to $z \to \infty$, but in the real ocean waves are reflected at the ocean surface and propagate back down. How does this
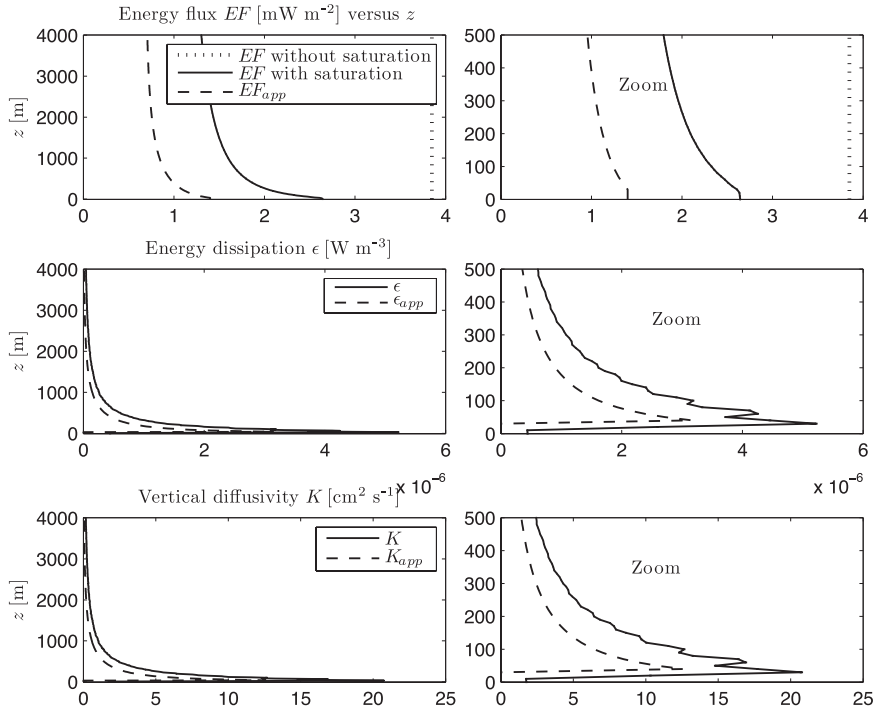

FIG. 14. Energy flux and implied mixing above random topography with MAR spectral slope and topography variance.
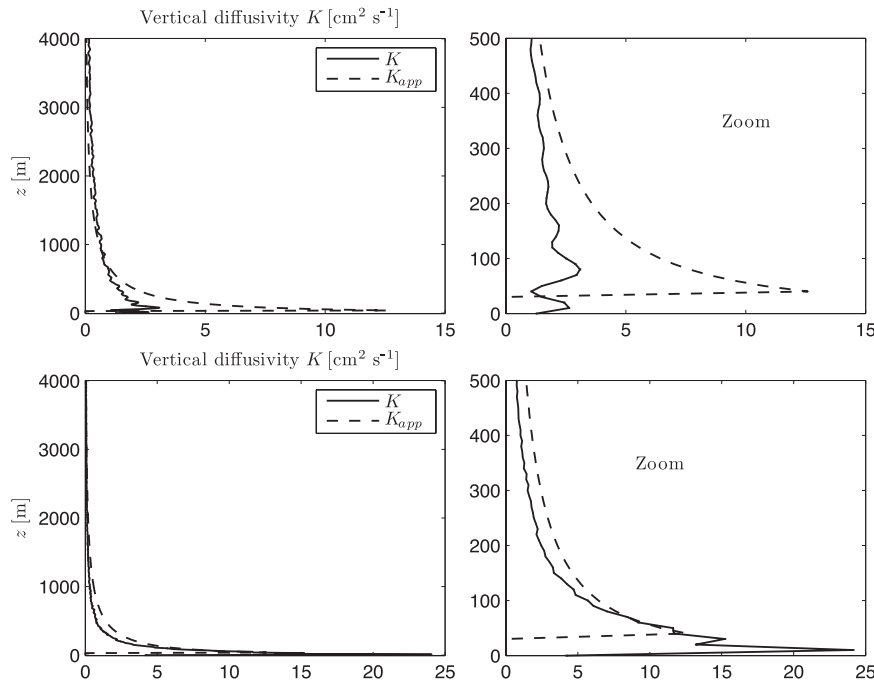
FIG. 15. Vertical diffusivity for Bell's spectrum with half and double high-wavenumber cutoff κ_2.

affect our results? In Muller (2008) we address this issue and derive a saturation scheme in an ocean of finite depth. Briefly, we mimic the initial value problem in an iterative method that yields the finite-depth solution as the steady state of upward- and downward-propagating waves. In other words, we compute the finite-depth solution as the sum of upward- and downward-propagating waves with vertical structures governed by the operators $G_{\mathrm{up}} = \mathrm{FT}^{-1}\{e^{-i\mu\kappa dz}\}$ and $G_{\mathrm{down}} = \mathrm{FT}^{-1}\{e^{+i\mu\kappa dz}\}$, respectively [note that for upward-propagating wave fronts we recover the infinite-depth operator G in (6)]. Then, to compute the saturated wave field, all we need to do is saturate the amplitude within each iteration at each z level and propagate the saturated amplitude up or down with the operator $G = \mathrm{FT}^{-1}\{e^{\pm i\mu\kappa dz}\}$.

New phenomena appear when the waves are allowed to reflect back from the surface. First, for isolated topography, any numerical solution using Fourier series on a bounded domain will include contributions from periodic duplicates of the topography, making the solution highly sensitive to the domain size (Fig. 16). Second, for periodic topography, the inviscid linear internal tides solution is ill posed. Both are related to the well-known ill posedness of the boundary value problem for time-periodic internal waves in bounded domains (e.g., Sobolev 1960; Maas and Lam 1995). This ill posedness can be seen from the solution in Fourier space

$$\hat{w}(\mathbf{k}, z) = \frac{\sin[\mu\kappa(H - z)]}{\sin(\mu\kappa H)}\hat{w}_0(\mathbf{k}),$$

where there is now the possibility for resonance with ocean normal modes when $\mu\kappa H$ is a multiple of π.

For isolated topography on an infinite domain, the problem can be made regular by adding dissipation along characteristics, which can be achieved by replacing κ by $\kappa(1 - i\epsilon)$ with a small positive ϵ that may depend on κ and then letting $\epsilon \to 0$ (see, e.g., Khatiwala 2003). Alternatively, one can study the well-posed initial value problem in which ω_0 is replaced by $\omega_0 + i\alpha$, where $\alpha > 0$ is a growth rate small compared to ω_0. This is also equivalent to applying an outward radiation condition as $|\mathbf{x}| \to \infty$ (Fig. 16a). In this case, the wave response is only found at resonant modes (see, e.g., Khatiwala 2003; Llewellyn Smith and Young 2002). In particular, finite depth suppresses all wave motions at scales larger than the first vertical mode $\kappa_1 = \pi/\mu H$. Numerically, the addition of small dissipation along the rays (Fig. 16b) fixes this ill posedness, and the iterative method described above applied to simple localized topographies yields energy fluxes consistent with previous estimates from Khatiwala (2003).

The case of periodic topography is not as clear. If the topography is not localized but periodic, such as the random topography of section 4, the rays from periodic duplicates are indeed part of the solution and need to be
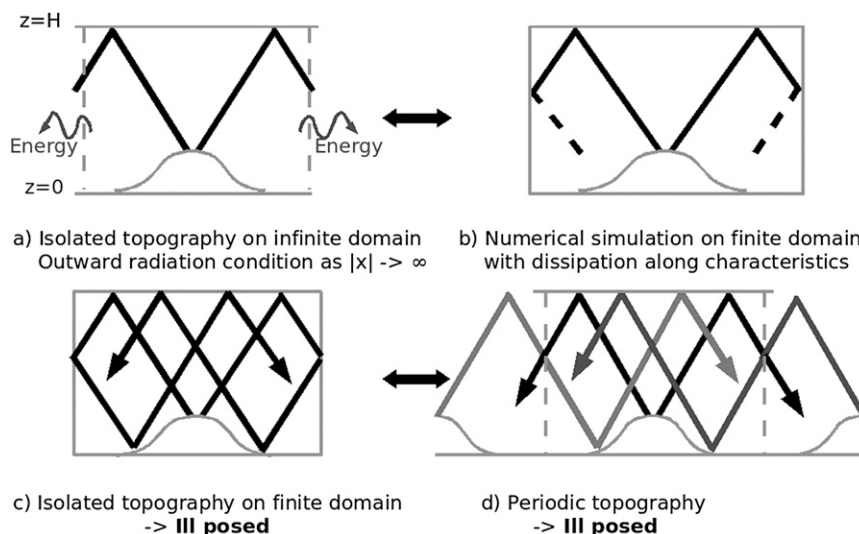
FIG. 16. Finite-depth solution: resonance and ill posedness.

retained. But without dissipation we find that the solution suffers from sensitive dependence to small changes in the domain size; the spatial structure of the waves is governed by a hyperbolic equation and does not depend smoothly on the domain size (Figs. 16c,d). Molecular viscosity is not enough to fix this ill posedness and the wave amplitudes computed for the random topography of section 4 are still unrealistically large. So what happens in the real ocean? Is wave generation above the Mid-Atlantic Ridge ill posed? It seems unphysical, or at least counterintuitive, that the wave field for Bell's homogeneous isotropic topographic spectrum would be dramatically sensitive to the domain size.

There are several oceanic processes that could fix this ill posedness in the real ocean. In fact, there seems to be six widely recognized dissipation mechanisms for the internal tides: direct rapid dissipation through convective and/or shear instabilities and vigorous associated turbulence (which we investigate in this paper), wave–wave interactions such as parametric subharmonic instability (PSI) (St. Laurent and Garrett 2002; Alford et al. 2007), scattering by the bathymetry (Müller and Xu 1992), scattering by mesoscale features (Rainville and Pinkel 2006), critical reflection (Kunze and Llewellyn Smith 2004; Cacchione et al. 2002), and scattering by the thermocline (Gerkema 2001). How much each contributes to dissipating the internal tides remains an open question and an active area of research. Topographic scattering has been investigated by Müller and Xu (1992) for random topography with Bell's spectrum; they find that less than 7% of the energy flux gets redistributed to higher modes at each scattering event.

This might be enough to fix the ill posedness, but PSI seems to be recognized as a more effective mechanism to move energy to higher modes (St. Laurent and Garrett 2002). PSI transfers energy from waves with tidal frequency ω_0 to waves with frequency $\omega_0/2$. Thus, for tidal frequencies, PSI is only effective at low latitudes, below $\approx 30°$ latitude for the M_2 tide. In Muller (2008), we use PSI to fix the ill posedness of the internal tides forced by random topography in an ocean of finite depth.

Surprisingly, the profiles of vertical diffusivities obtained are strikingly similar to the infinite-depth case (Muller 2008). The bottom value of the diffusivity is increased from about 12 to 15 cm^2 s^{-1}, which is likely due to waves reflecting back from the surface, but overall the vertical profiles obtained in a finite-depth ocean are in very good agreement with the infinite-depth case. This means that contributions from rays that reflect at the ocean surface do not seem to impact the vertical profile of diffusivity significantly. Actually, this is not so surprising since the presence of instabilities and mixing is dictated by the small-scale topography, for which the infinite-depth assumption is a reasonable assumption. The finiteness of the ocean is mostly felt by the low modes generated by large topographic features. So, for saturation, the infinite-depth approximation is fairly accurate and in practice one can use the simple saturation scheme from section 3 to estimate internal tides energy dissipation and induced mixing.

7. Concluding remarks

The generation of the internal tides is fairly well understood, but a clear understanding of their propagation

and dissipation is only emerging. Using a simple model for nonlinear wave saturation and breaking, we find profiles of vertical diffusivity for random topography consistent with oceanic measurements, decreasing from $\mathcal{O}(10\,\mathrm{cm^2\,s^{-1}})$ to $\mathcal{O}(1\,\mathrm{cm^2\,s^{-1}})$ within the first 500–600 m, and then decreasing to the background value of $0.1\,\mathrm{cm^2\,s^{-1}}$ higher up in the water column, above about 2 km from the seafloor. The bottom value depends on the small-scale spectrum of the topography; significant small-scale roughness leads to more intense bottom mixing. Although it is possible in theory to have geometric focusing of wave energy in the ocean interior (BM07), for a reasonable choice of random topography we find that most of the wave breaking occurs near the seafloor, and mostly upon generation since the profiles are unchanged when rays are allowed to reflect at the ocean surface and propagate back down. With topographies that contain significant small-scale roughness, the common small excursion approximation should not be used since it overestimates contributions from small scales and yields high unrealistic mixing values.

The current consensus seems to be that most of the energy flux radiates away as low modes, but our results indicate that as much as 60% of the energy flux could get dissipated within the first kilometer of the water column, of which 30% is lost directly at the generation site. Furthermore, vertical diffusivity decays faster than exponential near the bottom. Therefore, localized mixing above the seafloor could be more confined to the bottom and more intense than currently assumed. The ultimate fate of the internal tides that radiate away from the generation site remains an open question.

Arguably, the main result of this paper is that the presence of instabilities in the wave field is dictated by topographic scales below 10 km or so. St. Laurent and Garrett (2002) compute the cumulative energy flux spectrum at a site near the MAR; 50% of the energy flux is found at horizontal wavelengths below 15 km, and a third of the energy flux is at wavelengths below 10 km. Saturation could therefore induce significant energy loss. The current map of global bathymetry does not resolve such scales, which motivates the use of a statistical approach to represent the unresolved topography when addressing the role of internal tides in mixing the deep ocean.

APPENDIX

Amplitude for Tidal Ellipse

Tidal forces generate a barotropic tidal flow that is very close to elliptic (tidal ellipses above the MAR are shown in Fig. 9). In this appendix, we solve for the three-dimensional wave field generated by the interaction of this barotropic tide with the seafloor, using the same notations as in section 2. In particular, the horizontal coordinates and wavenumbers are respectively denoted $\mathbf{x} = (x, y)$ and $\mathbf{k} = (k, l)$, and we denote $|\mathbf{k}| = \kappa$.

It is convenient to work in the frame moving with the tidal flow $\boldsymbol{\xi} = (\xi, \eta) = \mathbf{x} - \int_0^t \mathbf{U}(\tau)\,d\tau$, where the vertical velocity satisfies (see Bell 1975a; Khatiwala 2003)

$$\left(f^2 + \frac{\partial^2}{\partial t^2}\right)\frac{\partial^2 w}{\partial z^2} + \left(N^2 + \frac{\partial^2}{\partial t^2}\right)\left(\frac{\partial^2 w}{\partial \xi^2} + \frac{\partial^2 w}{\partial \eta^2}\right) = 0.$$

To compute the bottom boundary condition, for simplicity we first assume that the x and y axes are aligned with the axes of the tidal ellipse, so $\mathbf{U}(t) = (U_0 \cos\omega_0 t, V_0 \sin\omega_0 t, 0)$ ($\alpha = 0$ in Fig. 10). The solution in an arbitrary frame can then easily be deduced from the solution in the tidal frame (see the end of this appendix). The derivation follows closely a computation by Bell (1978) in another context of advection by inertial oscillations in the mixed layer. The Fourier transform in $\boldsymbol{\xi}$ is related to the Fourier transform in $\mathbf{x}$ by $\hat{w}^\xi = \hat{w}e^{\imath\mathbf{k}\cdot\int_0^t \mathbf{U}(\tau)\,d\tau}$, and the bottom boundary condition becomes

$$\hat{w}^\xi(\mathbf{k}, z = 0, t) = \frac{\partial}{\partial t}\left[\hat{h}(\mathbf{k})e^{\imath\mathbf{k}\cdot\int_0^t \mathbf{U}(\tau)\,d\tau}\right]. \quad \text{(A1)}$$

Introducing β and θ such that $(kU_0/w_0, lV_0/w_0) = \beta(\cos\theta, \sin\theta)$, the boundary condition can be written

$$\hat{w}^\xi(\mathbf{k}, z = 0, t) = \hat{h}(\mathbf{k})\frac{\partial}{\partial t}\left(e^{\imath\beta[\sin(\omega_0 t - \theta) + \sin(\theta)]}\right), \quad \text{(A2)}$$

$$= \hat{h}(\mathbf{k})e^{\imath l V_0/\omega_0}\sum_{n\in\mathcal{Z}}J_n(\beta)\imath n\omega_0 e^{\imath n\omega_0 t}e^{-\imath n\theta}, \quad \text{(A3)}$$

where $J_n(x)$ is the Bessel function of the first kind of order n, and we have used $e^{\imath z \sin\theta} = \sum_{n\in\mathcal{Z}}J_n(z)e^{\imath n\theta}$ (Watson 1966).

So finally the vertical velocity has the form

$$w(x, z, t) = \sum_{n=1}^{n_0}\mathrm{Re}\left\{W_n\left[x - \int_0^t \boldsymbol{U}(\tau)\,d\tau, z\right]e^{-\imath n\omega_0 t}\right\}, \quad \text{(A4)}$$

where we only kept radiating modes; that is, n_0 is the largest integer strictly smaller than N/ω_0. The vertical structure of each mode is given by

$$W_n(x,z) = G_n(x,z) * W_n(x,0), \quad \hat{G}_n(k,z) = e^{-\imath\kappa\mu_n z} \quad \text{(A5)}$$

in an infinitely deep ocean and by

$$\hat{W}_n(k,z) = \frac{\sin[\mu_n\kappa(H-z)]}{\sin(\mu_n\kappa H)}\hat{W}_n(k,0) \quad \text{(A6)}$$

in an ocean of finite depth H, where $\mu_n = \sqrt{(N^2 - n^2\omega_0^2)/(n^2\omega_0^2 - f^2)}$. In both cases, the tidal ellipse enters the solution through its boundary condition

$$\hat{W}_n(k,0) = 2\hat{h}(k)(-1)^{n+1}\frac{J_n(\beta)}{\beta^n}\imath n\omega_0 e^{\imath l V_0/\omega_0}\left(\frac{kU_0 + ilV_0}{\omega_0}\right)^n, \quad \text{(A7)}$$

with $\beta = \sqrt{k^2U_0^2 + l^2V_0^2}/\omega_0$.

More generally, if the x and y axes make an angle α with the tidal ellipse (Fig. 10), the solution is unchanged except that the vector (k, l) is replaced by the wavenumber vector in the frame of the tidal ellipse $(K, L) = (k\cos\alpha - l\sin\alpha, k\sin\alpha + l\cos\alpha)$ in (A7).

REFERENCES

Alford, M. H., J. A. MacKinnon, Z. Zhao, R. Pinkel, J. Klymak, and T. Peacock, 2007: Internal waves across the Pacific. *Geophys. Res. Lett.*, **34**, L24601, doi:10.1029/2007GL031566.

Baines, P. G., 1973: The generation of internal tides by flat-bump topography. *Deep-Sea Res.*, **20**, 179–205.

Balmforth, N. J., G. R. Ierley, and W. R. Young, 2002: Tidal conversion by subcritical topography. *J. Phys. Oceanogr.*, **32**, 2900–2914.

Becker, J. J., and D. T. Sandwell, 2008: Global estimates of seafloor slope from single-beam ship soundings. *J. Geophys. Res.*, **113**, C05028, doi:10.1029/2006JC003879.

Bell, T. H., 1975a: Lee waves in stratified flows with simple harmonic time dependence. *J. Fluid Mech.*, **67**, 705–722.

——, 1975b: Statistical features of sea-floor topography. *Deep-Sea Res.*, **22**, 883–892.

——, 1975c: Topographically generated internal waves in the open ocean. *J. Geophys. Res.*, **80**, 320–327.

——, 1978: Radiation damping of inertial oscillations in the upper ocean. *J. Fluid Mech.*, **88**, 289–308.

Bühler, O., and C. J. Muller, 2007: Instability and focusing of internal tides in the deep ocean. *J. Fluid Mech.*, **588**, 1–28.

Cacchione, D. A., L. F. Pratson, and A. S. Ogston, 2002: The shaping of continental slopes by internal tides. *Science*, **296**, 724–727.

Cox, C., and H. Sandstrom, 1962: Coupling of internal and surface waves in water of variable depth. *J. Oceanogr. Soc. Japan*, **18**, 499–513.

Di Lorenzo, E., W. R. Young, and S. G. Llewellyn Smith, 2006: Numerical and analytical estimates of M_2 tidal conversion at steep oceanic ridges. *J. Phys. Oceanogr.*, **36**, 1072–1084.

Egbert, G. D., and R. D. Ray, 2000: Significant dissipation of tidal energy in the deep ocean inferred from satellite altimeter data. *Nature*, **405**, 775–778.

——, and ——, 2001: Estimates of M_2 tidal energy dissipation from TOPEX/Poseidon altimeter data. *J. Geophys. Res.*, **106**, 22 475–22 502.

Garrett, C., and E. Kunze, 2007: Internal tide generation in the deep ocean. *Annu. Rev. Fluid Mech.*, **39**, 57–87.

Gerkema, T., 2001: Internal and interfacial tides: Beam scattering and local generation of solitary waves. *J. Mar. Res.*, **59**, 227–255.

Goff, J. A., and T. H. Jordan, 1988: Stochastic modeling of seafloor morphology: Inversion of sea beam data for second-order statistics. *J. Geophys. Res.*, **93** (B11), 13 589–13 608.

Khatiwala, S., 2003: Generation of internal tides in an ocean of finite depth: Analytical and numerical calculations. *Deep-Sea Res.*, **50**, 3–21.

Kunze, E., and S. G. Llewellyn Smith, 2004: The role of small-scale topography in turbulent mixing of the global ocean. *Oceanography*, **17**, 51–60.

Ledwell, J. R., E. T. Montgomery, K. L. Polzin, L. C. St. Laurent, R. W. Schmitt, and J. M. Toole, 2000: Evidence for enhanced mixing over rough topography in the abyssal ocean. *Nature*, **403**, 179–182.

Legg, S., and K. Huijts, 2006: Preliminary simulations of internal waves and mixing generated by finite amplitude tidal flow over isolated topography. *Deep-Sea Res. II*, **53**, 140–156.

Llewellyn Smith, S. G., and W. R. Young, 2002: Conversion of the barotropic tide. *J. Phys. Oceanogr.*, **32**, 1554–1566.

——, and ——, 2003: Tidal conversion at a very steep ridge. *J. Fluid Mech.*, **495**, 175–191.

Maas, L. R. M., and F. P. A. Lam, 1995: Geometric focusing of internal waves. *J. Fluid Mech.*, **300**, 1–41.

Muller, C. J., 2008: Wave-induced mixing above the abyssal seafloor. Ph.D. thesis, New York University, 147 pp.

Müller, P., and N. Xu, 1992: Scattering of oceanic internal gravity waves off random bottom topography. *J. Phys. Oceanogr.*, **22**, 474–488.

Munk, W., and C. Wunsch, 1998: Abyssal recipes II: Energetics of tidal and wind mixing. *Deep-Sea Res. I*, **45**, 1977–2010.

Osborn, T., and C. Cox, 1972: Oceanic fine structure. *Geophys. Astrophys. Fluid Dyn.*, **3**, 321–345.

Petrelis, F., S. G. Llewellyn Smith, and W. R. Young, 2006: Tidal conversion at a submarine ridge. *J. Phys. Oceanogr.*, **36**, 1053–1071.

Polzin, K. L., J. M. Toole, J. R. Ledwell, and R. W. Schmitt, 1997: Spatial variability of turbulent mixing in the abyssal ocean. *Science*, **276**, 93–96.

Rainville, L., and R. Pinkel, 2006: Propagation of low-mode internal waves through the ocean. *J. Phys. Oceanogr.*, **36**, 1220–1236.

Robinson, R. M., 1969: The effect of a vertical barrier on internal waves. *Deep-Sea Res.*, **16**, 421–429.

Rudnick, D. L., and Coauthors, 2003: From tides to mixing along the Hawaiian Ridge. *Science*, **301**, 355–357.

Saenko, O. A., and W. J. Merryfield, 2005: On the effect of topographically enhanced mixing on the global ocean circulation. *J. Phys. Oceanogr.*, **35**, 826–834.

Samelson, R. M., 1998: Large-scale circulation with locally enhanced vertical mixing. *J. Phys. Oceanogr.*, **28**, 712–726.

Simmons, H. L., S. R. Jayne, L. C. St. Laurent, and A. J. Weaver, 2004: Tidally driven mixing in a numerical model of the ocean general circulation. *Ocean Modell.,* **6,** 245–263.

Smith, W. H. F., and D. T. Sandwell, 1997: Global sea floor topography from satellite altimetry and ship depth soundings. *Science,* **277,** 1956–1962.

Sobolev, S., 1960: On the motion of a symmetric top with a cavity filled by a fluid. *J. Appl. Mech. Tech. Phys.,* **3,** 20–55.

St. Laurent, L. C., and C. Garrett, 2002: The role of internal tides in mixing the deep ocean. *J. Phys. Oceanogr.,* **32,** 2882–2899.

——, H. L. Simmons, and S. R. Jayne, 2002: Estimating tidally driven mixing in the deep ocean. *Geophys. Res. Lett.,* **29,** 2106.

——, S. Stringer, C. Garrett, and D. Perrault-Joncas, 2003: The generation of internal tides at abrupt topography. *Deep-Sea Res. I,* **50,** 987–1003.

Thorpe, S., 2005: *The Turbulent Ocean.* Cambridge University Press, 439 pp.

Toole, J. M., R. W. Schmitt, and K. L. Polzin, 1994: Estimates of diapycnal mixing in the abyssal ocean. *Science,* **264,** 1120–1123.

Watson, G. N., 1966: *A Treatise on the Theory of Bessel Functions.* 2nd ed. Cambridge University Press, 405 pp.

Wunsch, C., 2000: Moon, tides and climate. *Nature,* **405,** 743–744.

——, and R. Ferrari, 2004: Vertical mixing, energy, and the general circulation of the oceans. *Annu. Rev. Fluid Mech.,* **36,** 281–314, doi:10.1146/annurev.fluid.36.050802.122121.